Nanoscale

PAPER

View Article Online
View Journal | View Issue

Cite this: *Nanoscale*, 2018, **10**, 791

Upconverting nanocomposites with combined photothermal and photodynamic effects†

Yue Huang, [a] Artiom Skripka, [a] Lucía Labrador-Páez, [b] Francisco Sanz-Rodríguez, [b,c] Patricia Haro-González, [b] Daniel Jaque, [b,c] Federico Rosei [a,d,e] and Fiorenzo Vetrone *[a,d,e]

Lanthanide-doped upconverting nanoparticles (UCNPs) have been studied for diverse biomedical applications due to their inherent ability to convert near-infrared (NIR) excitation light to higher energies (spanning the ultraviolet, visible, and NIR regions). To explore additional functionalities, rational combination with other optically active nanostructures may lead to the development of new multimodal nanoplatforms with theranostic (therapy and diagnostic) capabilities. Here, we develop a nanocomposite consisting of $NaGdF_4$:Er^{3+}, Yb^{3+} UCNPs, mesoporous silica (SiO_2), gold nanorods (GNRs) and a photosensitizer, with integrated functionalities including luminescence imaging, photothermal generation, nanothermometry and photodynamic effects. Under 980 nm irradiation, GNRs and UCNPs are simultaneously excited due to the overlap between the surface plasmon resonance of the GNRs and the absorption of the UCNPs leading to plasmonic enhancement of the upconverted luminescence, while concomitantly creating a temperature gradient. The temperature increase can be determined from the intensity ratio of the upconverted green emission of the UCNPs. Finally, a photosensitizer, zinc phthalocyanine, was loaded into the mesoporous SiO_2. Upon laser irradiation, the upconverted visible light subsequently activates the photosensitizer to release reactive oxygen species. The multifunctional GNR@SiO_2@UCNPs nanocomposites showed strong luminescence signal when incubated in HeLa cervical cancer cells, making them ideal bioprobes for future theranostic applications.

Received 26th July 2017,
Accepted 3rd December 2017

DOI: 10.1039/c7nr05499h

rsc.li/nanoscale

Introduction

In recent years, lanthanide (Ln^{3+})-doped upconverting nanoparticles (UCNPs) have been intensively investigated, largely focusing on potential applications such as nanoscale thermometry, diagnostics and therapy. In particular, significant research has focused on their use as multifunctional nanoscale platforms with combined therapeutic and diagnostic (theranostic) modalities.[1–3] The rising interest in UCNPs stems from their unorthodox excitation schemes where they can be excited with near-infrared (NIR) light and ultimately emit higher energy photons spanning the ultraviolet (UV), visible and NIR regions *via* a multiphoton excitation process, known as upconversion.[4–6] The upconverted (or anti-Stokes) luminescence of UCNPs is advantageous when compared with conventional (Stokes) fluorescence from other nanomaterials, for several reasons. The NIR excitation light causes minimal photodamage, induces practically no autofluorescence background, and can penetrate biological tissues to a much greater extent.[7,8] As an added benefit, some of the upconverted Ln^{3+} emission bands are sensitive to the surrounding temperatures, thereby allowing them to be effectively used as thermal nanoprobes (nanoscale thermometers also known as nanothermometers). One of the most well-known examples of an optical nanothermometer exploits the temperature sensitive emissions of the Er^{3+} ion. In particular, the relative intensity of the two green emission bands emanating from the $^2H_{11/2}$ and $^4S_{3/2}$ excited states of Er^{3+} change as a function of temperature. Consequently, Er^{3+}-doped UCNPs have been used as non-contact, non-invasive optical nanothermometers to measure the temperature of living cells.[9,10]

In parallel to research on UCNPs, a significant body of work has focused on applying the heat generation capabilities of

[a]*Institut National de la Recherche Scientifique (INRS), Centre Énergie, Matériaux et Télécommunications, Université du Québec, 1650 Boulevard Lionel-Boulet, Varennes, Québec J3X 1S2, Canada. E-mail: vetrone@emt.inrs.ca*
[b]*Fluorescence Imaging Group, Departamento de Física de Materiales, Facultad de Ciencias, Universidad Autónoma de Madrid, Madrid, 28049, Spain*
[c]*Instituto Ramón y Cajal de Investigación Sanitaria, Hospital Ramón y Cajal, Madrid, 28034, Spain*
[d]*Institute of Fundamental and Frontier Science, University of Electronic Science and Technology of China, Chengdu, 610051, China*
[e]*Centre for Self-Assembled Chemical Structures, McGill University, Montréal, H3A 2K6, Canada*

†Electronic supplementary information (ESI) available: Supplementary figures. See DOI: 10.1039/c7nr05499h

certain nanostructures, such as noble metal nanoparticles, for the photothermal therapy of cancer (also known as hyperthermia).[11–13] Metal nanoparticles possess a high optical absorption coefficient and thermal dissipation rate, which is desired for highly efficient photothermal therapy (PTT). This allows these nanostructures to efficiently convert photon energy into heat following laser irradiation of their surface plasmon resonance (SPR), the resonant oscillation of conduction electrons at the metal interface, subsequently resulting in the controlled death of surrounding cells.[14,15] Among metal nanostructures for PTT, gold nanorods (GNRs) are considered to be one of the most promising and versatile platforms.[16–18] GNRs with fine-tuned optical properties can be excited by NIR light and simultaneously exhibit excellent photothermal conversion effects due to high surface-to-volume ratios and can thus generate efficient and localized hyperthermia.[19] However, excess use of cetyltrimethylammonium bromide (CTAB) as a bilayer stabilizer around the GNR surface during their preparation would restrict their clinical application, resulting from the cytotoxicity caused by the CTAB capping molecules.[20] To address this challenge, surface functionalization of GNRs has been investigated to further their potential in nanomedicine-based theranostic approaches.[21] Mesoporous silica (SiO_2) is an excellent option for surface functionalization and has been successfully used to coat GNRs. This mesoporous coating not only reduces the cytotoxicity and aggregation of GNRs, but also imparts drug (or cargo) loading ability while providing an excellent scaffold for subsequent chemical modification of the surface with additional moieties.[22,23]

The combination of these two optically excited nanostructures onto a single nanoplatform could lead to additional functionalities. For instance, controlling temperature in hyperthermia applications is a critical factor preventing healthy cells from also being destroyed (and consequently inducing severe side effects).[24] Thus, coupling the nanoheaters with "built-in" nanothermometers would minimize the possibility of destroying healthy tissue surrounding the hyperthermia target and accordingly, the patient's side effects. In addition, when UCNPs and GNRs are in close proximity, it has been previously demonstrated that their interaction could influence the luminescence intensity of the UCNPs. For example, if the SPR of the GNRs was tuned to the excitation frequency of UCNPs (typically 980 nm, if Yb^{3+} is used as a sensitizer), the local electromagnetic field would become much larger and the luminescence intensity would be enhanced.[25] For this enhancement to occur, the distance between plasmonic metal nanoparticles and UCNPs is critical and using SiO_2 as a spacer, for example, would lead to a noticeable enhancement of the upconverted luminescence intensity.[26,27]

Recently, additional functionalities could be attained from UCNPs through rational combination with other optically active nanostructures, resulting in promising multi-modal nanoplatforms combining therapeutic and diagnostic actions.[28–30] In this work, we developed a multifunctional nanocomposite based on the combination of UCNPs with GNRs, prepared through a layer-by-layer assembly. The GNR cores were coated with a mesoporous SiO_2 shell, which was decorated with $NaGdF_4$:Er^{3+}, Yb^{3+} UCNPs. This multifunctional nanocomposite is ideal for controlled photothermal heating since both the nanoheaters (GNRs at the core) and the nanothermometers (UCNPs decorated on the surface of the SiO_2) can be excited in the NIR region at 980 nm. To add further functionality, zinc phthalocyanine (ZnPc) was loaded into the mesoporous layer. ZnPc, a model photodynamic therapy (PDT) drug has been shown to have high cytotoxic efficiency in cancer cells due to the generation of reactive oxygen species (ROS) including singlet oxygen following light excitation.[31,32] Typically, ZnPc and its analogues are excited with visible light, which restricts its deployment in clinical cancer treatments due to the limited penetration depth of the excitation light. By employing UCNPs, this inherent drawback could be overcome since they can convert tissue penetrating NIR excitation light to visible, which can then be absorbed by the photosensitizer (ZnPc) thereby triggering the release of ROS for application in the photodynamic therapy of cancer. Here, we investigate the luminescence properties of these new GNR@SiO_2@UCNPs nanoplatforms and study their ability for controlled photoheating/nanothermometry and photodynamic effects. Finally, we also investigated the cytotoxicity of this nanocomposite. The multifunctional nanocomposite developed here could not only be well suited for bioimaging, but also for future multi-pronged cancer theranostics through the combination of imaging, nanothermometry as well PTT and PDT effects.

Experimental section

Materials

The lanthanide oxides (Ln_2O_3 (99.99%), Ln = Gd, Yb, Er), trifluoroacetic acid (99%), sodium trifluoroacetate (98%), oleic acid (90%), 1-octadecene (90%), hydrogen tetrachloroaurate(III) hydrate ($HAuCl_4{\cdot}3H_2O$), cetyltrimethylammonium bromide (CTAB, 98%), silver nitrate ($AgNO_3$, >99%), L-ascorbic acid ($C_6H_8O_6$, >99%), 5-bromosalicylic acid (>98.0%), zinc phthalocyanine (ZnPc, 95%) were purchased from Alfa Aesar. Sodium borohydride ($NaBH_4$, 99.99%), 3-aminopropyltriethoxysilane (APTES, 99%), 9,10-anthracenediyl-bis(methylene)dimalonic acid (ABDA), Triton™ X-100 were purchased from Sigma Aldrich. Ultrapure deionized water (Millipore system) was used throughout the experiments. All starting chemicals in this work were used without further purification.

Synthesis of $(CF_3COO)_3Ln$ (Ln = Gd, Yb, Er) precursors

In a typical synthesis of the lanthanide trifluoroacetate precursors, 0.975 mmol (353.4 mg) Gd_2O_3, 0.025 mmol (9.6 mg, 2 mol% doping rate) Er_2O_3, and 0.25 mmol (98.5 mg, 20 mol% doping rate) Yb_2O_3 were mixed in a 100 mL three-neck round-bottom flask with 5 mL distilled water and 5 mL trifluoroacetic acid, followed by refluxing under magnetic stirring at 80 °C until a clear solution was obtained. Subsequently, the temperature was reduced to 60 °C to evaporate the residual trifluoroacetic acid and water. The dried precursor was isolated in the form of a colorless powder.

Synthesis of $NaGdF_4:Er^{3+}$, Yb^{3+} UCNPs

For the synthesis of $NaGdF_4:Er^{3+}$, Yb^{3+} UCNPs, 2.5 mmol (340 mg) sodium trifluoroacetate as well as 20 mL 1-octadecene, 10 mL oleic acid and 10 mL oleylamine were added to the obtained $(CF_3COO)_3Ln$ precursor. Subsequently, the mixture was degassed for 30 min at 100 °C under vacuum and magnetic stirring. The reaction mixture was then heated to 240 °C under stirring with a gentle argon flow and maintained at this temperature for 2 h. Subsequently, the solution was allowed to cool to room temperature and the resultant oleate-capped UCNPs were precipitated with ethanol and collected by centrifugation. The obtained product was washed three times with hexane/ethanol (4 : 1) and dispersed in 5 mL hexane as stock solution.

Oleate-citrate ligand exchange

To obtain water dispersible UCNPs, ligand exchange was carried out as previously described in the literature.[33] 60 mg of oleate-capped $NaGdF_4:Er^{3+}$, Yb^{3+} UCNPs obtained from the previous step were dispersed in 5 mL of hexane, and mixed with 5 mL of a 0.2 M trisodium citrate buffer (adjusted to pH 4). The mixture was kept on a shaker for 3 h, and subsequently transferred into a separation funnel, from which the aqueous phase containing the $NaGdF_4:Er^{3+}$, Yb^{3+} was collected. The UCNPs were precipitated with acetone (1 : 5 aqueous : organic ratio), collected by centrifugation and re-dispersed in 5 mL of trisodium citrate buffer (adjusted to pH 7). The dispersion was placed on the shaker for an additional 2 h. Finally, the UCNPs were precipitated with acetone, washed three times with acetone and water, collected by centrifugation and dispersed in 2 mL of water for further experiments.

Preparation of gold nanorods (GNRs)

The seed solution for GNRs was prepared as reported previously.[34] 5 mL of 0.5 mM $HAuCl_4$ was mixed with 5 mL of 0.2 M CTAB solution. Subsequently, 0.60 mL of ice-cold 0.010 M $NaBH_4$ was added under vigorous stirring, which resulted in a color change from yellow to brownish-yellow. The seed solution was kept at room temperature before use.

For the growth solution preparation, 0.36 g of CTAB together with 0.044 g of 5-bromosalicylic acid was dissolved in 10 mL of deionized water. With the solution at 30 °C, 0.60 mL of 4 mM $AgNO_3$ was added and kept undisturbed for 15 min. Subsequently, 10 mL of 1 mM $HAuCl_4$ was added, and 0.084 mL HCl (37 wt%) was added. After 15 min of slow stirring, 80 μL of 0.064 M ascorbic acid was slowly added to the mixture. The final step was the addition of 32 μL of the seed solution to the growth solution causing a gradual color change of the solution. The temperature of the growth solution was kept constant at 30 °C during the entire procedure.

Preparation of silica coated GNRs ($GNR@SiO_2$)

To remove excess CTAB surfactant, the synthesized GNRs were washed by centrifugation and the sample was dispersed in 10 mL of deionized water. After that, 100 μL of 0.1 M NaOH was added. Following this step, three 30 μL injections of 20% TEOS in methanol were added under gentle stirring at 30 min intervals. The mixture was left to react for 2 days.

APTES functionalized $GNR@SiO_2$

The solution of $GNR@SiO_2$ was centrifuged and suspended in ethanol. Then, 20 μL of APTES was added and mixed by gentle shaking for another 6 h to accomplish the aminolization. Finally, the sample was centrifuged and washed with ethanol.

UCNPs attachment to $GNR@SiO_2$

The APTES functionalized $GNR@SiO_2$ was added drop wise to the solution of UCNPs under vigorous stirring. After 2 h, the final product ($GNR@SiO_2$@UCNPs) was centrifuged out, and then redispersed either in ethanol or water for further characterization.

Measurement of singlet oxygen ($^1O_2$)

The $^1O_2$ production was detected by singlet oxygen sensors using 9,10-anthracenediyl-bis(methylene) dimalonic acid (ABDA).[35] Different samples in phosphate buffer (PBS) (pH 7–7.4) were mixed with ABDA (10 μM) and placed in a cuvette. The solution was irradiated by a 980 nm laser for different periods of time, and the generation of $^1O_2$ resulted in the bleaching of ABDA absorption at 380 nm.

Cellular viability

The cell viability was investigated in HeLa cervical cancer cells. The cells were seeded onto 96-well plates with a density of 1×10^4 cells per well and incubated at 37 °C for 48 h. After cell attachment, different samples were added to the wells and subsequently incubated additionally at 37 °C for 24 h. Cell viability was measured using the 3-(4,5-dimethylthiazol-2-yl)-2,5-diphenyltetrazolium bromide (MTT) assay.[36]

Fluorescence cell image

For fluorescence imaging of HeLa cells incubated with $GNR@SiO_2$@UCNPs, they were seeded in 6-well plates containing sterile cover slips and were kept in a sterile environment for 24 h. Then, cells were exposed to incubation with $GNR@SiO_2$@UCNPs for 4 h at 37 °C. Subsequently, the cells were fixed with 3.5% formaldehyde in PBS for 20 min at 4 °C. Once they were washed three times with PBS, the cells were scanned using an in house designed confocal microscope (Fig. S1†). Laser excitation was performed using a 980 nm diode laser coupled to a single mode fiber (LU0975M500 model from LUMICS GmbH). The 980 nm laser radiation was first collimated and then focused into the HeLa cancer cell using a 100× 0.85 NA microscope objective. The fluorescence generated by the $GNR@SiO_2$@UCNPs incorporated into the cells was collected by the same microscope objective. This collected luminescence, after passing through different filters was spectrally analyzed by a monochromator (iH320, Horiba) and recorded with a high sensitivity Si CCD camera (Synapse, Horiba). The system was optimized for the analysis of the green emission of erbium (Er^{3+}) ions at approxi-

mately 550 nm. The HeLa cells were mounted on a 0.1 μm resolution XY stage such that it was possible to scan the HeLa cells with respect to the 980 nm laser spot.

Characterization

The crystalline phase of all nanostructures under investigation was analyzed by X-ray diffraction (XRD, Bruker D8 Advanced Diffractometer, Cu Kα radiation). Dynamic light scattering (DLS, Malvern, Zetasizer Nano S90) was used to determine the hydrodynamic diameter of the nanostructures. The morphology and size distribution of the GNRs and UCNPs were determined with a Philips CM200 high-resolution transmission electron microscope (HR-TEM), equipped with an energy-dispersive X-ray (EDX) unit. The UV-Visible (UV-VIS) absorption spectra were obtained using a UV-VIS spectrometer (Varian Cary 5000). Luminescent measurements were carried out under 980 nm excitation using a laser diode (Thorlabs fiber-coupled laser 305 diode). The laser beam was focused on the sample using a lens to obtain a spot with a Gaussian intensity distribution with a 0.4 mm diameter. The emitted light was collected by a lens in a 90° configuration, and then transferred to a spectrophotometer (Avaspec-2048L-USB2) using an optical fiber.

Results and discussion

Preparation and characterization of GNR@SiO_2@UCNPs

To prepare the multifunctional nanocomposites based on UCNPs and GNRs with combined luminescence, photodynamic and photothermal properties for potential use in theranostics, a layer-by-layer procedure was employed. This multifunctional nanocomposite contains a mesoporous SiO_2 layer separating the UCNPs decorated on the surface and the GNR core, which has multiple roles. First, it is used as a scaffold for the attachment of the UCNPs. Second, it acts as a spacer to separate the plasmonic nanostructure (GNR) and the fluorescent species (UCNPs) leading to minimal luminescence quenching and potentially, plasmonic enhancement. Finally, the pores can be loaded with photosensitizer molecules capable of transforming the upconverted visible radiation to ROS (*i.e.* $^1O_2$) adding another modality to the nanoplatform. To prepare this nanocomposite, a multistep synthetic method was proposed and summarized in Scheme 1. Initially, the $NaGdF_4$:Er^{3+}, Yb^{3+} UCNPs were synthesized by the previously described thermal decomposition method.[37] As seen in Fig. 1A, the synthesized UCNPs were monodisperse and uniform with an average diameter of approximately 6.5 nm. The HR-TEM image of the UCNPs is shown in the Fig. 1B and the lattice fringes were clearly observed with a spacing of ~0.275 nm, ~0.317 nm assigned to the {200}, {111} planes of cubic (α-) phase $NaGdF_4$:Er^{3+}, Yb^{3+} UCNPs, respectively. This result is consistent with XRD studies (Fig. 2B), which confirmed that the UCNPs crystallized in the α-phase, and no impurity crystalline phase was found in the diffraction pattern. Separately, GNRs were prepared according to a previously published protocol[38] and their morphology and average size were imaged by TEM (Fig. 1C). GNRs with an average of 72 nm in length and 12 nm in diameter were successfully synthesized, yielding an aspect ratio of

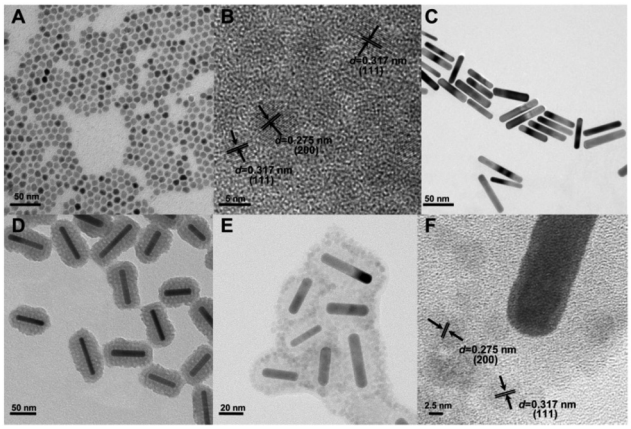

Fig. 1 (A) TEM and (B) HR-TEM images of the synthesized $NaGdF_4$:Er^{3+}, Yb^{3+} UCNPs. TEM images of the (C) synthesized GNRs, (D) the SiO_2 coated GNRs (GNR@SiO_2), and (E) the hybrid SiO_2 coated GNRs decorated with $NaGdF_4$:Er^{3+}, Yb^{3+} UCNPs (GNR@SiO_2@UCNPs), (F) HR-TEM image of the GNR@SiO_2@UCNPs interface.

Scheme 1 Schematic illustration of the synthetic procedure for the preparation of the GNR@SiO_2@UCNPs nanocomposite.

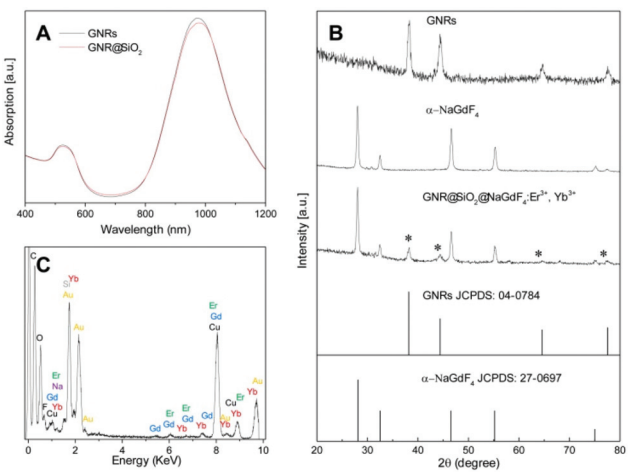

Fig. 2 (A) Extinction spectra of GNRs and GNR@SiO_2. (B) XRD patterns of GNRs, α-$NaGdF_4$:Er^{3+}, Yb^{3+}, hybrid nanocomposite of GNRs and $NaGdF_4$:Er^{3+}, Yb^{3+} (GNR@SiO_2@UCNPs). The standard pattern of pure GNRs (JCPDS file No: 04-0784), pure α-$NaGdF_4$ (JCPDS file No: 27-0697) are provided for reference. The stars show the diffraction peaks of GNRs in the GNR@SiO_2@UCNPs nanocomposite. (C) Elemental analysis of hybrid GNRs@SiO_2@UCNPs nanocomposite by EDX.

approximately 6 : 1. To characterize the GNRs' absorption properties, a key parameter in the photogeneration of heat, their SPR was investigated using UV-VIS absorption spectroscopy. We observed the presence of two SPR absorption bands around 525 and 972 nm, due to the transverse and longitudinal plasmon absorptions, respectively (Fig. 2A). Subsequently, the SiO_2 layer was grown on the surface of the GNRs[39] where CTAB served as the organic template for the formation of the mesoporous SiO_2 layer with a thickness of *ca.* 15 nm (see Fig. 1D), offering the opportunity for loading of the therapeutic photosensitizer molecules, and providing significant spacing between the GNRs and UCNPs that can facilitate plasmon enhanced upconversion emission intensity. Following the growth of the SiO_2 layer, the longitudinal SPR of the GNR@SiO_2 nanostructures exhibited a small red-shift (~11 nm), to 983 nm (Fig. 2A), overlapping perfectly with the 980 nm excitation wavelength.

After functionalization of the SiO_2 coated GNRs using 3-aminopropyltriethoxylsilane (APTES), they were mixed together with the citrate-capped UCNPs. At pH 6 of the colloidal solution, the amino group of the APTES was fully protonated (NH^{4+}), whereas the UCNPs possessed negative charge (cit^{-}). Hence, electrostatic forces between the UCNPs and APTES functionalized GNR@SiO_2 allowed for their surface decoration. DLS results (Fig. S2†) show that the hydrodynamic diameter of the nanocomposites reaches 142 nm, which is larger than that of GNR@SiO_2 (122 nm). This additionally indicates that UCNPs are in fact attached onto the surface of GNR@SiO_2 nanostructures. Fig. 1E shows the morphology of the SiO_2 coated GNRs following attachment of the UCNPs as well as the interface between the UCNPs and GNR@SiO_2 as characterized by HR-TEM. As shown in Fig. 1F, two lattice fringes from the $NaGdF_4$:Er^{3+}, Yb^{3+} UCNPs were visible, with spacing of ~0.275 nm corresponding to the {200} planes and the larger lattice spacing of ~0.317 nm matching the {111} crystal planes of the α-$NaGdF_4$:Er^{3+}, Yb^{3+} UCNPs. The assembly of the hybrid nanocomposite composed of $NaGdF_4$:Er^{3+}, Yb^{3+} UCNPs and GNRs could be further confirmed by XRD (Fig. 2B). The main diffraction peaks coincided well with the pure α-phase $NaGdF_4$ crystal (JCPDS No: 27-0697) and face-centered cubic (fcc) structure of metallic Au (JCPDS No: 04-0784). In addition, compositional analysis by energy-dispersive X-ray microanalysis (EDX) indicated that Na, Gd, F, Yb, Er, Au, and Si elements were present in this hybrid nanocomposite (Fig. 2C), further confirming that it consists of GNR@SiO_2 and UCNPs.

Photoluminescence properties of the GNR@SiO_2@UCNPs

The upconversion mechanism as well as the energy state diagrams of Yb^{3+} and Er^{3+} ions are illustrated schematically in Fig. S3 of the ESI.† It is well known that $NaGdF_4$:Er^{3+}, Yb^{3+} UCNPs possess a large absorption at 980 nm and can be efficiently excited *via* a continuous wave NIR laser to induce the upconversion process. In this mechanism, the Yb^{3+} ions (the sensitizers) are excited from the ground state ($^2F_{7/2}$) to the excited state ($^2F_{5/2}$) and then undergo subsequent energy transfers to the Er^{3+} ions (the activators) in close proximity. This excites the Er^{3+} ions from the ground state ($^4I_{15/2}$) to the first intermediate excited state ($^4I_{11/2}$) and further to the $^4F_{7/2}$ excited state. Following multiphonon (non-radiative) decay, the lower energy $^2H_{11/2}$ and $^4S_{3/2}$ emitting states are populated, which produce the green emission at 525 and 545 nm through radiative decay from the $^2H_{11/2}$ and $^4S_{3/2}$ excited states to the $^4I_{15/2}$ ground state, respectively. Alternatively, the excited Er^{3+} ions in the $^4S_{3/2}$ excited state can further decay non-radiatively to the lower-lying $^4F_{9/2}$ excited state producing the observed red emission at approximately 660 nm from the radiative transition of the $^4F_{9/2}$ excited state to the ground state. However, the $^4F_{9/2}$ excited state can also be populated by direct energy transfer. In this case, once the Er^{3+} ion is excited to the $^4I_{11/2}$ intermediate state following the first energy transfer from an excited Yb^{3+} ion, it can also undergo non-radiative decay from the $^4I_{11/2}$ excited intermediate state to the lower $^4I_{13/2}$ state. A transfer of energy from another excited Yb^{3+} ion in the $^2F_{5/2}$ state in close proximity can then directly populate the red $^4F_{9/2}$ emitting state.

Previous reports have demonstrated that the upconverted emission intensity could be used to monitor changes in temperature of the environment.[9,10] For Er^{3+} ions, given that the difference in energy between the $^2H_{11/2}$ and $^4S_{3/2}$ excited states is only several hundred wavenumbers (cm^{-1}), the lower energy $^4S_{3/2}$ state could easily thermally populate the upper $^2H_{11/2}$ state. Therefore, the populations of the $^2H_{11/2}$ and $^4S_{3/2}$ states are in thermal equilibrium and the relative intensity of these two excited states will vary as a function of temperature. This ratio can therefore be exploited for temperature sensing applications and is generally referred to as the Luminescence Intensity Ratio (LIR) technique. Thus for thermometry applications, the relative intensity ratio between the $^2H_{11/2} \rightarrow {}^4I_{15/2}$ and $^4S_{3/2} \rightarrow {}^4I_{15/2}$ emission bands could be calculated based on the Boltzmann distribution

$$R = C \exp\left(\frac{-\Delta E}{kT}\right) \quad (1)$$

Where R represents the LIR of the $^2H_{11/2} \rightarrow {}^4I_{15/2}$ and $^4S_{3/2} \rightarrow {}^4I_{15/2}$, C is a constant, ΔE is the energy gap between the two excited states ($^2H_{11/2}$ and $^4S_{3/2}$), k is the Boltzmann constant, and T is the absolute temperature. Fig. 3A presents two upconversion emission spectra (excited at 980 nm) of the UCNPs at two different temperatures, 20 and 60 °C. Comparing both distinct bands between 515–535 nm and 535–570 nm, the ratio increases with temperature, and this ratio increment follows a linear relation with temperature, as can be observed in the graph in Fig. 3B. In this case, the experimental determination of this ratio yields a direct temperature measurement. This increase in the ratio between the corresponding emitting peak intensities could therefore be employed for thermal sensing.[9,40] Afterwards, based on this ratio, the same procedure was followed to estimate the temperature of the GNR@SiO_2@UCNPs hybrid nanocomposite sample.

From the detailed analysis of data in Fig. 3C, the ratio of the upconversion intensity between the upconverted

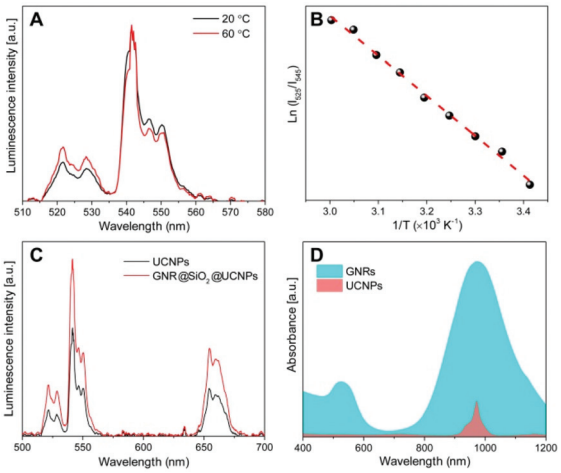

Fig. 3 (A) Normalized upconversion luminescence spectra of UCNPs at two different temperatures. (B) The temperature dependence of the ratio calculated from the luminescence spectra obtained at various temperatures. Dots are experimental results and the red line is the best linear fit. (C) Upconversion luminescence spectra of UCNPs and GNR@SiO_2@UCNPs. (D) Normalized absorption spectra of UCNPs and GNRs.

515–535 nm and 535–570 nm emissions of the GNR@SiO_2@UCNPs nanocomposite clearly increases when compared with that of the bare UCNPs at the same conditions. The thermal change of the GNR@SiO_2@UCNPs nanocomposites under NIR excitation was determined by the previously obtained linear regression equation for the $NaGdF_4$: Er^{3+}, Yb^{3+} UCNPs. Under NIR excitation of 0.8 W the temperature in the excitation area of 0.4 mm in diameter, changed by approximately 1.0 and 7.3 °C for UCNPs alone and GNR@SiO_2@UCNPs nanocomposites, respectively (Fig. S4†). In turn, this shows that the UCNPs attached to the surface of GNRs can be successfully used for real-time temperature sensing at the nanoscale, particularly for precise control of photothermal effect. Meanwhile, it is worth noting that the nanocomposites are quite stable after laser excitation, since the same luminescence intensity and heating properties could be observed after several cycles of laser irradiation, which demonstrates that UCNPs are not lost from the surface of GNR@SiO_2 and no morphological changes occur to the GNRs (they retain their rod-like morphology). In this nanocomposite, the GNRs could therefore easily be used as nanoscale heaters when excited at 980 nm, while the UCNPs decorated on the surface of the SiO_2 shell effectively behave as thermal sensors. Moreover, the total emission from the Er^{3+} ions in the GNR@SiO_2@UCNPs nanocomposite was enhanced when compared with bare UCNPs. This is due to the fact that when the SPR of the GNRs overlaps with the excitation of the UCNPs ($^2F_{5/2}$ from Yb^{3+} and $^4I_{11/2}$ from Er^{3+} at 980 nm), as shown in Fig. 3D, the energy harnessed by the plasmonic nanostructures (GNRs) could be transferred to the electrons of the Ln^{3+} dopants in the UCNPs, resulting in an increase in their absorption cross-section.[25,41] Further to this, the SPR can affect the upconversion luminescence depending on the relative position of the SPR from the excitation or emission of UCNPs as well as the distance separating the UCNPs from the metal surface, that is to say, the thickness of the spacer layer between the UCNPs and the surface of the GNRs.[42] There are three competitive effects that contribute to this behavior: the plasmonic field causing luminescence enhancement, the radiative decay rate from coupling of the upconversion emission with the SPR of the GNRs resulting in luminescence enhancement and the non-radiative energy transfer resulting in luminescence quenching. In this study, the SPR (980 nm) of the GNRs was far away from the upconversion emission, therefore, the radiative decay rate played a negligible role. If the fluorescent species (UCNPs) are close to the metal surface, the upconversion luminescence decreases, as the non-radiative energy transfer is dominant. With the increase of the distance between the two species (*i.e.* the thickness of the spacer layer in this case SiO_2), the plasmonic field enhancement becomes dominant leading to the observed increase of the UCNP luminescence.

Characterization of ZnPc loaded GNR@SiO_2@UCNPs and photodynamic effect

The photosensitizer ZnPc was selected as candidate to be loaded into the mesoporous silica and to deliver the desired photodynamic effect. A concentrated solution of ZnPc was mixed together with the GNR@SiO_2@UCNPs until the ZnPc was absorbed into the porous SiO_2. The ZnPc loading capacity was determined by the UV-VIS spectra and reached 1.8% (w/w). Meanwhile, the luminescence intensity of ZnPc loaded GNR@SiO_2@UCNPs under NIR laser irradiation was also investigated and it was observed that a quenching of the luminescence occurred after ZnPc was loaded into the GNR@SiO_2@UCNPs nanocomposite (Fig. 4A). In fact, the red emission ($^4F_{9/2} \rightarrow {}^4I_{15/2}$) of the GNR@$SiO_2$@UCNPs from Er^{3+} decreased by 54%, which was significantly more than the decrease in green emission (29%). This quenching resulted from efficient energy transfer between the UCNPs (energy donors) and the ZnPc molecules (energy acceptors) due to the favorable spectral overlap between the red emission of the UCNPs at 660 nm and the absorption of ZnPc at 665 nm (Fig. 4B). In addition, the ratio of the green emission bands discussed above remains almost unchanged after ZnPc loading in the GNR@SiO_2@UCNPs nanocomposites indicating that the LIR technique can still be used for thermal sensing after loading.

The capacity of ROS production, in particular singlet oxygen ($^1O_2$), was assessed using ABDA as a probe molecule. As shown in Fig. 4C, three control groups were studied, ABDA incubated with ZnPc loaded GNR@SiO_2@UCNPs without NIR laser irradiation (blue triangles), ZnPc molecules with NIR laser irradiation (black squares), and GNR@SiO_2@UCNPs alone with NIR laser irradiation (red circles). No significant changes are observed for these control groups over time, which indicates that no $^1O_2$ generation occurred. However, for ABDA incubated with ZnPc loaded GNR@SiO_2@UCNPs follow-

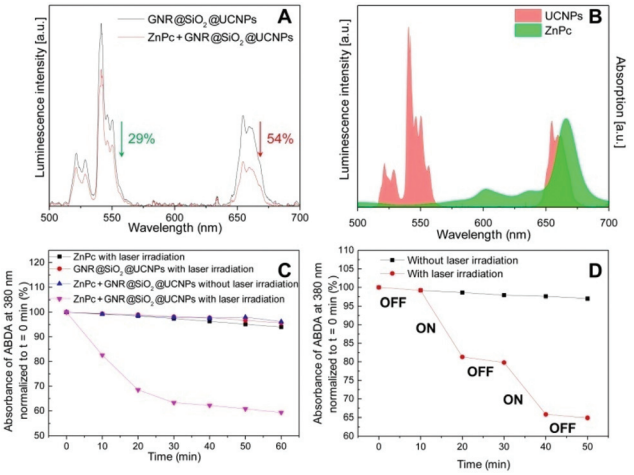

Fig. 4 (A) Upconversion luminescence spectra of GNR@SiO_2@UCNPs and ZnPc loaded GNR@SiO_2@UCNPs under 980 nm laser irradiation. (B) Upconversion emission spectrum of $NaGdF_4$:Er^{3+}, Yb^{3+} UCNPs and UV-VIS absorption spectrum of ZnPc, indicating the partial spectral overlap between the ZnPc absorption and the UCNP emission. (C) Production of $^1O_2$ under consumption of ABDA for different samples over time. (D) Production of $^1O_2$ under consumption of ABDA in the absence and presence of laser irradiation.

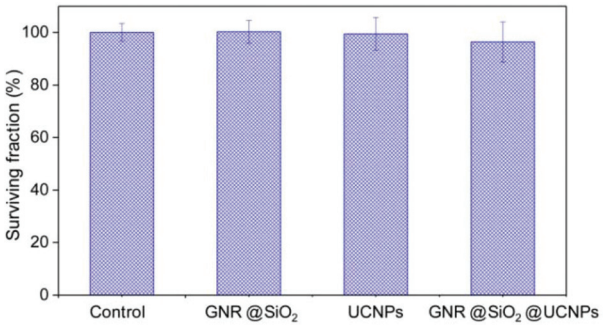

Fig. 5 Percent survival of HeLa cancer cells incubated for a period of 24 h with GNR@SiO_2, UCNPs and GNR@SiO_2@UCNPs. Each point corresponds to the mean value ± SD from three different experiments.

ing NIR laser irradiation, the absorbance of ABDA decreased significantly demonstrating that both ZnPc molecules and GNR@SiO_2@UCNPs nanocomposites as well as 980 nm laser irradiation are necessary for the generation of $^1O_2$. To further confirm that $^1O_2$ production is triggered by laser irradiation, as shown in Fig. 4D, the suspension of ZnPc loaded GNR@SiO_2@UCNPs was exposed to laser irradiation cycles of 10 minutes and the results clearly revealed that the $^1O_2$ generation was reduced when the laser was switched off. Similar results were observed when the laser cycling was repeated. This enhanced $^1O_2$ production upon laser irradiation could be attributed to the photodynamic process: UCNPs were excited by laser irradiation, and the emitted luminescence was absorbed by ZnPc molecules in the pores, subsequently generating reactive and cytotoxic oxygen species (ROS) that can eventually be exploited for cancer treatment.

In vitro cytotoxicity and imaging

To study the potential application of our multifunctional nanoplatforms for *in vitro* studies at the cellular level, both their cytotoxicity and capacity for cell labelling and imaging were studied. Firstly, the cytotoxicity of the UCNPs, GNR@SiO_2 and GNR@SiO_2@UCNPs was investigated by MTT assay on HeLa cervical cancer cells. The result in Fig. 5 demonstrates that there is no significant decrease in the cell viability of the UCNPs and GNR@SiO_2 samples at a concentration of 50 μg ml^{-1}. Compared with UCNPs and GNR@SiO_2, a slightly higher cytotoxicity was observed after cell incubation with the GNR@SiO_2@UCNPs nanocomposites; a surviving fraction of *ca.* ~96.3% was observed after incubation for 24 h at a concentration of 50 μg ml^{-1}. This slightly lower viability may be attributed to the positively APTES capped GNR@SiO_2 nanostructures, which could lead to the cellular cytotoxicity in terms of causing mitochondrial and lysosomal damage.[43,44]

Once the low cytotoxicity of the multifunctional platforms was evidenced, we proceeded with cell imaging studies. In doing so, HeLa cells were incubated with a solution containing the GNR@SiO_2@UCNPs nanocomposites. Incubation time was set to 24 h. After incubation, cells were washed and placed in the confocal microscope. The 980 nm focal plane was set to match the axial location of the HeLa cells and these were scanned while recording the emission spectra in the 500–580 nm spectral range. A typical bright field (BF) optical image of an individual HeLa cell is included in Fig. 6A. The spatial variation of the green fluorescence intensity obtained when the 980 nm laser was scanned over the HeLa cell of Fig. 6A is shown in Fig. 6B. When both fluorescence and BF optical images are merged (see Fig. 6C) it is clear that the GNR@SiO_2@UCNPs nanocomposites are incorporated within the HeLa cell since the luminescence signal is very well localized inside the cell. This suggests that the GNR@SiO_2@UCNPs nanocomposites have been accumulated at a well-defined location inside the cell. This is in good agreement with previous

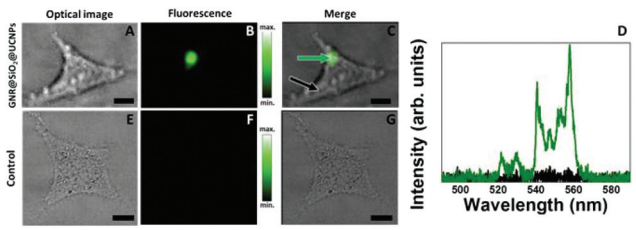

Fig. 6 (A) BF optical image of a HeLa cancer cell incubated for a period of 24 h with GNR@SiO_2@UCNPs. (B) Fluorescence image obtained by scanning the 980 nm laser spot over the HeLa cell in (A) and by recording the emitted intensity in the 500–580 nm spectral range. (C) Merge of optical and fluorescence images denoting accumulation of GNR@SiO_2@UCNPs inside the HeLa cell. (D) Emission spectra as obtained at two different locations inside the cell denoted by green and black arrows in (C). (E), (F), and (G) are the BF optical image, microluminescence map, and merged image of a HeLa cell for control, respectively. Scale bars: 10 μm.

work.[45] It has been stated that agglomeration of UCNPs inside HeLa cells could take place for long incubation times (as in our case). This effect is a consequence of the intracellular transportation of nutrients from the cellular membrane to the Golgi apparatus. To verify that the green emission collected was generated by the GNR@SiO_2@UCNPs nanocomposites, the emission spectra were recorded at two different locations inside the HeLa cell. Results are shown in Fig. 6D. When compared with the emission spectra included in Fig. 3 and 4, it is clearly observed that the fluorescence image was generated by the GNR@SiO_2@UCNPs nanocomposites. Control experiments, by using HeLa cells incubated in a medium dispersion without GNR@SiO_2@UCNPs nanocomposites were also conducted, revealing the complete absence of fluorescence contrast (see Fig. 6E–G).

Conclusions

In summary, a GNR@SiO_2@UCNPs nanocomposite was synthesized and characterized. We studied the photothermal generation as well as the luminescence properties of the GNR@SiO_2@UCNPs and observed that after NIR excitation at 980 nm, significant heating was produced from the plasmonic GNRs at the core of the nanocomposite. It was determined that the ratio of the intensities of the green upconverted emission between the $^2H_{11/2} \rightarrow {}^4I_{15/2}$ and $^4S_{3/2} \rightarrow {}^4I_{15/2}$ transitions from the UCNPs functionalized on the surface of the mesoporous SiO_2 shell surrounding the GNR cores changed as a function of temperature and could be exploited for thermal sensing resulting in a nanocomposite with both photothermal generation capabilities and real time temperature monitoring. Moreover, the total luminescence intensity of the UCNPs was increased in the presence of GNRs (compared to the UCNPs alone) and this enhancement was attributed to the overlap of the excitation of the UCNPs with the SPR of the GNRs at 980 nm as well to the mesoporous SiO_2 between the UCNPs and GNR acting as a spacer to mitigate any non-radiative energy transfer between the plasmonic GNR and the luminescent UCNPs. Thus, the luminescence of the UCNPs was influenced by the localized electromagnetic field created by the GNRs, which leads to the observed enhancement in the luminescence intensity. ZnPc was selected as a photosensitizer to load into the mesoporous SiO_2 layer and a quenching of the UCNPs was observed following loading of the pores. This demonstrated that the emitted upconverted luminescence was effectively absorbed by the ZnPc molecules, which subsequently generated the ROS. Finally, *in vitro* cell experiments were performed to assess the cytotoxicity of GNRs@SiO_2@UCNPs. Results showed the absence of any cytotoxicity on the incubated cells thus determining that they were excellent biocompatible nanocomposites. Similarly, cell labeling experiments were performed and it was determined that the GNR@SiO_2@UCNPs nanocomposites accumulated at a well-defined location inside the HeLa cells and were imaged *via* the upconverted green luminescence from inside the cells. These results confirm that GNR@SiO_2@UCNPs have the potential to be used as NIR-excited multifunctional nanoplatforms for theranostic applications, specifically due to their photothermal and photodynamic capabilities.

Conflicts of interest

There are no conflicts to declare.

Acknowledgements

F. V. and F. R. acknowledge funding from the Natural Sciences and Engineering Research Council (NSERC Discovery Grants) of Canada and Fonds de Recherche du Québec-Nature et technologies (FRQNT) for supporting this research. F. V. also is grateful to the Fondation Sibylla Hesse for funding. Y. H. acknowledges financial support from the Merit Scholarship Program for Foreign Students from the Ministère de l'Éducation, du Loisir et du Sport du Québec. F. R. is grateful to the Canada Research Chairs program for partial salary support and acknowledges NSERC for an EWR Steacie Memorial Fellowship. F. R. is also grateful to the Government of China for a Chang Jiang Scholar Short Term Award and to Sichuan Province for a 1000 talent short term award. L. L.-P., P. H.-G., and D. J. acknowledge the Spanish Ministerio de Educación y Ciencia (MAT2013-47395-C4-1-R and MAT2016-75362-C3-1-R) and the EU Framework Programme (COST Action CM1403) for supporting this research. L. L.-P. also thanks the Universidad Autónoma de Madrid for the "Formación de Personal Investigador (FPI-UAM)" program. P. H.-G. is grateful to the Spanish Ministerio de Economia y Competitividad (MINECO) for the Juan de la Cierva program.

Notes and references

1 J. Zhou, Q. Liu, W. Feng, Y. Sun and F. Y. Li, *Chem. Rev.*, 2015, **115**, 395–465.
2 G. Y. Chen, H. L. Qju, P. N. Prasad and X. Y. Chen, *Chem. Rev.*, 2014, **114**, 5161–5214.
3 F. Wang, D. Banerjee, Y. S. Liu, X. Y. Chen and X. Liu, *Analyst*, 2010, **135**, 1839–1854.
4 F. Auzel, *Chem. Rev.*, 2004, **104**, 139–174.
5 H. Dong, L. D. Sun and C. H. Yan, *Nanoscale*, 2013, **5**, 5703–5714.
6 J. A. Capobianco, F. Vetrone, T. D'Alesio, G. Tessari, A. Speghini and M. Bettinelli, *Phys. Chem. Chem. Phys.*, 2000, **2**, 3203–3207.
7 J. Zhou, Z. Liu and F. Y. Li, *Chem. Soc. Rev.*, 2012, **41**, 1323–1349.
8 E. Hemmer, A. Benayas, F. Légaré and F. Vetrone, *Nanoscale Horiz.*, 2016, **1**, 168–184.
9 F. Vetrone, R. Naccache, A. Zamarron, A. J. de la Fuente, F. Sanz-Rodriguez, L. M. Maestro, E. M. Rodriguez,

D. Jaque, J. G. Sole and J. A. Capobianco, *ACS Nano*, 2010, **4**, 3254–3258.
10 D. Jaque and F. Vetrone, *Nanoscale*, 2012, **4**, 4301–4326.
11 D. Jaque, L. Martínez Maestro, B. del Rosal, P. Haro-Gonzalez, A. Benayas, J. L. Plaza, E. Martín Rodrígueza and J. García Solé, *Nanoscale*, 2014, **6**, 9494–9530.
12 L. Cheng, C. Wang, L. Z. Feng, K. Yang and Z. Liu, *Chem. Rev.*, 2014, **14**, 10869–10939.
13 C. D. Brites, P. P. Lima, N. J. O. Silva, A. Millán, V. S. Amaral, F. Palacio and L. D. Carlos, *Nanoscale*, 2012, **4**, 4799–4829.
14 P. K. Jain, X. H. Huang, I. H. El-Sayed and M. A. El-Sayed, *Acc. Chem. Res.*, 2008, **41**, 1578–1586.
15 N. S. Abadeer and C. J. Murphy, *J. Phys. Chem. C*, 2016, **120**, 4691–4716.
16 A. M. Alkilany, L. B. Thompson, S. P. Boulos, P. N. Sisco and C. J. Murphy, *Adv. Drug Delivery Rev.*, 2012, **64**, 190–199.
17 X. H. Huang, S. Neretina and M. A. El-Sayed, *Adv. Mater.*, 2009, **21**, 4880–4910.
18 Z. J. Zhang, J. Wang and C. Y. Chen, *Theranostics*, 2013, **3**, 223–238.
19 G. Baffou, R. Quidant and C. Girard, *Appl. Phys. Lett.*, 2009, **94**, 153109.
20 A. M. Alkilany, P. K. Nagaria, C. R. Hexel, T. J. Shaw, C. J. Murphy and M. D. Wyatt, *Small*, 2009, **5**, 701–708.
21 E. Locatelli, I. Monaco and M. C. Franchini, *RSC Adv.*, 2015, **5**, 21681–21699.
22 Z. J. Zhang, L. M. Wang, J. Wang, X. M. Jiang, X. H. Li, Z. J. Hu, Y. H. Ji, X. C. Wu and C. Y. Chen, *Adv. Mater.*, 2012, **24**, 1418–1423.
23 S. Shen, H. Y. Tang, X. T. Zhang, J. F. Ren, Z. Q. Pang, D. G. Wang, H. L. Gao, Y. Qian, X. G. Jiang and W. L. Yang, *Biomaterials*, 2013, **34**, 3150–3158.
24 A. J. Gormley, N. Larson, S. Sadekar, R. Robinson, A. Ray and H. Ghandehari, *Nano Today*, 2012, **7**, 158–167.
25 W. Park, D. Lu and S. Ahn, *Chem. Rev.*, 2015, **44**, 2940–2962.
26 F. Zhang, G. B. Braun, Y. F. Shi, Y. C. Zhang, X. H. Sun, N. O. Reich, D. Y. Zhao and G. Stucky, *J. Am. Chem. Soc.*, 2010, **132**, 2850–2851.
27 W. Ge, X. R. Zhang, M. Liu, Z. W. Lei, R. J. Knize and Y. L. Lu, *Theranostics*, 2013, **3**, 282–288.
28 R. Lv, P. Yang, B. Hu, J. Xu, W. Shang and J. Tian, *ACS Nano*, 2017, **11**, 1064–1072.
29 A. Skripka, R. Marin, A. Benayas, P. Canton, E. Hemmer and F. Vetrone, *Phys. Chem. Chem. Phys.*, 2017, **19**, 11825–11834.
30 R. Lv, P. Yang, F. He, S. Gai, G. Yang, Y. Dai, Z. Hou and J. Lin, *Biomaterials*, 2015, **63**, 115–127.
31 G. Valduga, E. Reddi, S. Garbisa and G. Jori, *Int. J. Cancer*, 1998, **75**, 412–417.
32 C. N. Zhou, S. J. Chi, J. S. Deng, J. L. Liang, G. Jori and C. Milanesi, *J. Photochem. Photobiol., B*, 1996, **33**, 219–223.
33 Y. Huang, E. Hemmer, F. Rosei and F. Vetrone, *J. Phys. Chem. B*, 2016, **120**, 4992–5001.
34 B. Nikoobakht and M. A. El-Sayed, *Chem. Mater.*, 2003, **15**, 1957–1962.
35 T. Zhao, H. Wu, S. Q. Yao, Q. H. Xu and G. Q. Xu, *Langmuir*, 2010, **26**, 14937–14942.
36 F. Denizot and R. Lang, *J. Immunol. Methods*, 1986, **89**, 271–277.
37 H. X. Mai, Y. W. Zhang, R. Si, Z. G. Yan, L. D. Sun, L. P. You and C. H. Yan, *J. Am. Chem. Soc.*, 2006, **128**, 6426–6436.
38 X. Ye, L. Jin, H. Caglayan, J. Chen, G. Xing, C. Zheng, V. Doan-Nguyen, Y. Kang, N. Engheta, C. R. Kagan and C. B. Murray, *ACS Nano*, 2012, **6**, 2804–2817.
39 I. Gorelikov and N. Matsuura, *Nano Lett.*, 2008, **8**, 369–373.
40 Y. Huang, F. Rosei and F. Vetrone, *Nanoscale*, 2015, **7**, 5178–5185.
41 M. Saboktakin, X. C. Ye, U. K. Chettiar, N. Engheta, C. B. Murray and C. R. Kagan, *ACS Nano*, 2013, **7**, 7186–7192.
42 M. Saboktakin, X. Ye, S. J. Oh, S. H. Hong, A. T. Fafarman, U. K. Chettiar, N. Engheta, C. B. Murray and C. R. Kagan, *ACS Nano*, 2012, **6**, 8758–8766.
43 E. Frohlich, *Int. J. Nanomed.*, 2012, **7**, 5577–5591.
44 S. Bhattacharjee, L. H. J. de Haan, N. M. Evers, X. Jiang, A. T. M. Marcelis, H. Zuilhof, I. M. C. M. Rietjens and G. M. Alink, *Part. Fibre Toxicol.*, 2010, **7**, 25.
45 F. Vetrone, R. Naccache, A. J. de la Fuente, F. Sanz-Rodriguez, A. Blazquez-Castro, E. M. Rodriguez, D. Jaque, J. G. Sole and J. A. Capobianco, *Nanoscale*, 2010, **2**, 495–498.